Chaotic Dirac Billiard in Graphene Quantum Dots

L. A. Ponomarenko,[1] F. Schedin,[1] M. I. Katsnelson,[2] R. Yang,[1] E. W. Hill,[1] K. S. Novoselov,[1]* A. K. Geim[1]

The exceptional electronic properties of graphene, with its charge carriers mimicking relativistic quantum particles and its formidable potential in various applications, have ensured a rapid growth of interest in this new material. We report on electron transport in quantum dot devices carved entirely from graphene. At large sizes (>100 nanometers), they behave as conventional single-electron transistors, exhibiting periodic Coulomb blockade peaks. For quantum dots smaller than 100 nanometers, the peaks become strongly nonperiodic, indicating a major contribution of quantum confinement. Random peak spacing and its statistics are well described by the theory of chaotic neutrino billiards. Short constrictions of only a few nanometers in width remain conductive and reveal a confinement gap of up to 0.5 electron volt, demonstrating the possibility of molecular-scale electronics based on graphene.

One of the most discussed and tantalizing directions in research on graphene (*1*, *2*) is its use as the base material for electronic circuitry that is envisaged to consist of nanometer-sized elements. Most attention has so far been focused on graphene nanoribbons (*3*–*12*). An alternative is quantum dot (QD) devices that, as described below, can be made entirely from graphene, including their central islands (CIs), quantum barriers, source and drain contacts, and side-gate electrodes.

Our experimental devices were microfabricated from graphene crystallites prepared by cleavage on top of an oxidized Si wafer (300 nm of SiO_2) (*1*). By using high-resolution electron-beam lithography, we defined a 30-nm-thick polymethylmethacrylate (PMMA) mask that protected chosen areas during oxygen plasma etching and allowed us to carve graphene into a desired geometry. The inset in Fig. 1A shows one of our working devices that generally consisted of the CI of diameter D, connected via two short constrictions to wide source and drain regions; the devices also had side-gate electrodes [we often placed them ~1 μm away from the CI as explained in (*13*)]. The Si wafer was used as a back gate. The constrictions were designed to have equal length and width of 20 nm (*13*), and we refer to them as quantum point contacts (QPCs). They provided quantum barriers to decouple the CI from the contacts (*14*, *15*). If necessary, by using further etching (after the devices were tested), we could narrow QPCs by several nm, exploiting the gradual etching away of the PMMA mask not only from top but also sideways. This allowed us to tune the resistance of QDs to a value of several hundred kilohm, i.e., much larger than resistance quantum h/e^2 (e is the electron charge, and h is Planck's constant), which is essential for single-electron transport. Graphene QDs with features as small as 10 nm could be fabricated reliably with this approach. For even smaller D, irregularities in PMMA [~5 nm (*16*)] became comparable in size with the designed features and, unavoidably on this scale, we could only estimate the device geometry. The measurements were carried out using the standard lock-in technique with dc bias at temperatures T from 0.3 to 300 K. We used both side and back gates; the latter allowed extensive changes in the population of QD levels, whereas the former was useful for accurate sweeps over small energy intervals (*13*). The response to the side-gate potential differed for different devices but could be related to back-gate voltage V_g through a numerical factor. For consistency, all the data are presented as a function of V_g.

We have found three basic operational regimes for QDs, depending on their D. Our large devices exhibit (nearly) periodic Coulomb blockade (CB) resonances that at low T are separated by regions of zero conductance G (Fig. 1A). As T increases, the peaks become broader and overlap, gradually transforming into CB oscillations (Fig. 1B). The oscillations become weaker as G increases with carrier concentration or T, and completely disappear for G larger than $\sim 0.5e^2/h$ because the barriers become too transparent to allow CB. For the data in Fig. 1B, we have identified more than 1000 oscillations. Their periodicity, $\Delta V_g \approx 16$ mV, yields the capacitance between the back gate and CI, $C_g = e/\Delta V_g \approx 10$ aF, which is close to $C_g \approx 2\varepsilon_0(\varepsilon + 1)D \approx 20$ aF, as expected for a disk placed on top of SiO_2 (dielectric constant $\varepsilon \approx 4$) and at a distance $h \geq D = 250$ nm from the metallic Si gate (in this case, C_g is nearly the same as for an isolated disk) (*17*). The difference by a factor of 2 can be accounted for in terms of screening by the contact regions (*17*).

The overall shape of the conductance curve $G(V_g)$ in Fig. 1B resembles that of bulk graphene but is distorted by smooth (on the scale of ΔV_g) fluctuations that are typical for mesoscopic devices and are due to quantum interference (*1*–*4*, *18*–*20*). Smooth variations in the CB peak height (Fig. 1A) are attributed to interference-induced changes in the barriers' transparency, as shown by studying individual QPCs (*13*). Furthermore, we have measured the dependence of CB on applied bias V_b and, from the standard stability diagrams (Coulomb diamonds), found the charging energy E_c. The lower inset in Fig. 1B shows such diamonds for $D \approx 250$ nm, which yields $E_c \approx 3$ meV and the total capacitance $C = e^2/E_c \approx 50$ aF. The rather large E_c implies that the CB oscillations in Fig. 1B

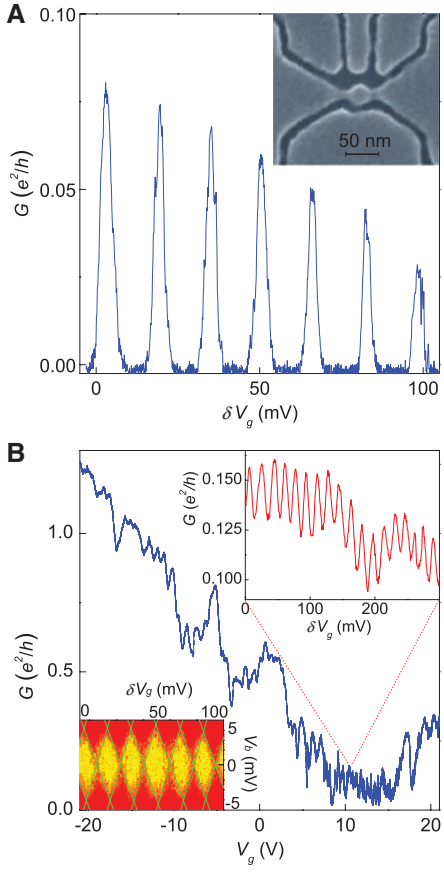

Fig. 1. Graphene-based single-electron transistor. (**A**) Conductance G of a device with the central island of 250 nm in diameter and distant side gates (*13*) as a function of V_g in the vicinity of +15 V (B); $T = 0.3$ K. The inset shows one of our smaller devices to illustrate the high resolution of our lithography that allows features down to 10 nm. Dark areas in the scanning electron micrograph are gaps in the PMMA mask so that graphene is removed from these areas by plasma etching. In this case, a 30-nm QD is connected to contact regions through narrow constrictions and there are four side gates. (**B**) Conductance of the same device as in (A) over a wide range of V_g ($T = 4$ K). Upper inset: Zooming into the low-G region reveals hundreds of CB oscillations. The lower inset shows Coulomb diamonds: differential conductance $G_{diff} = dI/dV$ as a function of V_g (around +10 V) and bias V_b (yellow-to-red scale corresponds to G_{diff} varying from zero to $0.3e^2/h$).

[1]Manchester Centre for Mesoscience and Nanotechnology, University of Manchester, Manchester M13 9PL, UK. [2]Institute for Molecules and Materials, Radboud University Nijmegen, 6525 ED Nijmegen, Netherlands.

*To whom correspondence should be addressed. E-mail: novoselov@manchester.ac.uk

are smeared mostly due to an increase in the barrier transparency with T, and submicrometer graphene QDs should be operational at $T \geq 10$ K. In general, the observed behavior is in agreement with the one exhibited by conventional single-electron transistors (SETs). Such devices were previously studied with metallic and semiconducting materials (*14*, *15*) and, more recently, the first SETs made from graphite (*18*) and graphene (*1*, *19*, *20*) were also demonstrated. The all-graphene SETs reported here are technologically simple, reliable, and robust and can operate well above liquid-helium T, making them attractive candidates for use in various charge-detector schemes (*14*).

For devices smaller than ~100 nm, we observed a qualitative change in behavior: CB peaks were no longer a periodic function of V_g but varied strongly in their spacing (Fig. 2, A and B, illustrate this behavior for $D \approx 40$ nm, whereas Fig. 2C plots the distance ΔV_g between the nearest peaks for 140 of them). One can see that ΔV_g varies by a factor of 5 or more, which exceeds by orders of magnitude typical variations of ΔV_g observed in nongraphene QDs (*15*, *21*, *22*). This is a clear indication that the size quantization becomes an important factor even for such a modest confinement. The reason for this is that a typical level spacing $\delta E \approx v_F h/2D$ for graphene's massless carriers [Dirac fermions (*1*, *2*)] in a quantum box of size D is much larger than $\delta E \approx h^2/8mD^2$ for massive carriers in other materials ($v_F \approx 10^6$ m/s is the Fermi velocity in graphene, and m is the effective mass). The distance between CB peaks is determined by the sum of charging and confinement energies $\Delta E = E_c + \delta E$, and the latter contribution becomes dominant for our devices with $D < 100$ nm. Accordingly, we refer to them as QDs rather than SETs (*23*). Because E_c is constant for a given QD geometry, variations in ΔE (found from the height of Coulomb diamonds) are due to confinement, which allows us to estimate characteristic δE (*24*). For example, we find $\delta E \sim 10$ meV for the 40-nm QD (Fig. 2), in agreement with the above formula $\delta E \approx \alpha/D$, where coefficient α varies around 0.5 eV·nm by a factor of 2 in different models (*5*–*12*).

For four devices with different D, we have carried out statistical analysis of their peak spacing (Fig. 3). As QDs become smaller, the average distance $\langle \Delta V_g \rangle$ between CB peaks gradually increases (Fig. 2A; inset). General expectations suggest that $\langle \Delta V_g \rangle$ should be proportional to $1/D$, being determined by two contributions to the QD capacitance: geometrical and quantum (*15*). According to the formula used above, the geometrical capacitance is $\propto D$. The quantum capacitance is given by the confinement energy and, in the first approximation, is also expected to vary as D. Indeed, it has been shown (*25*) that energy levels E_{nl} of Dirac fermions inside a disk of diameter D are described by $J_l(E_{nl}D/2\hbar v_F) = J_{l+1}(E_{nl}D/2\hbar v_F)$, where n and l are the main and orbital quantum numbers, respectively, and $J_l(x)$ are the Bessel functions. This equation yields a typical level splitting $\langle \delta E \rangle \propto 1/D$ (*25*), in qualitative agreement with the behavior of $\langle \Delta V_g \rangle$ in Fig. 2A.

However, further analysis reveals that the above simple picture starts to break down for $D <$ 100 nm. One can see from Fig. 3 that the shape of the spectral distribution notably changes: For small QDs, the histograms become increasingly broader, as compared to their average positions. Also, $\langle \Delta V_g \rangle$ changes somewhat quicker than $1/D$ (Fig. 2A, inset). We have calculated statistical deviations $\delta(\Delta V_g)$ from the average $\langle \Delta V_g \rangle$ and found that $\delta(\Delta V_g)$ grows approximately as $1/D^2$ with decreasing D (Fig. 2A). For example, for $D \approx 40$ nm, average fluctuations in the peak spacing become as large as $\langle \Delta V_g \rangle$ itself, which essentially means random positions of CB peaks. The observed behavior contradicts the one expected for Dirac fermions confined inside an ideal disk (*25*).

To explain this discrepancy, we point out that any confinement of Dirac fermions, except for the circular one, is predicted to result in quantum chaos (even the simplest square geometry leads to chaotic trajectories) (*25*). In general, chaos is a common feature of all systems with several degrees of freedom, whose behavior cannot be described as a superposition of independent one-dimensional motions. Classically, this entanglement between different variables leads to an exponential increase in the distance between two initially close trajectories with increasing time. Quantum mechanically, chaotic systems are characterized by distinctive statistics of their energy levels, which must comply with one of the Gaussian random ensembles, in contrast to the level statistics for the nonchaotic systems described by the Poisson distribution (*26*).

The experimentally observed level statistics in graphene QDs agrees well with the one predicted for chaotic Dirac or "neutrino" billiards (Fig. 3). Indeed, in our case, the quantum capacitance is no longer $\propto D$ because δE changes as $\propto 1/D^2$ (*25*), reflecting the lifting of the level

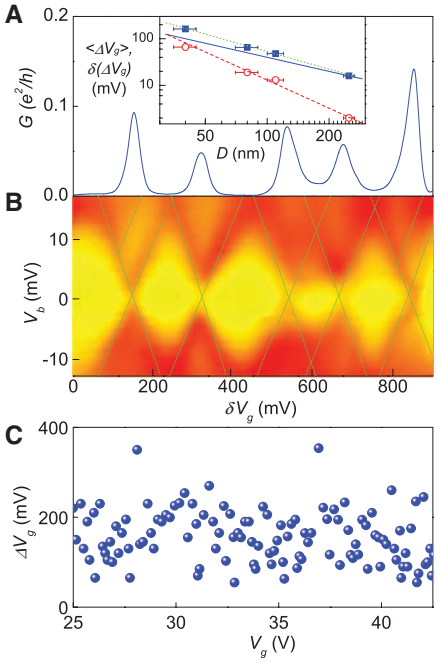

Fig. 2. Effect of quantum confinement. CB peaks (**A**) and Coulomb diamonds (**B**) for a 40-nm QD (T = 4 K). Variations in peak spacing and the size of diamonds are clearly seen. Yellow-to-red scale in (B) corresponds to G_{diff} varying from zero to $0.4e^2/h$. Two excited states (marked by additional lines) are feebly visible around $\delta V_g \approx 150$ and 850 mV and $V_b \approx 10$ mV. The smearing is caused by an increase in the transparency of quantum barriers at higher V_b. Further examples of excited states are given in the supporting material (*13*). (**C**) Separation of nearest-neighbor peaks at zero V_b in the same device for a large interval of V_g (beyond this interval, CB became suppressed by high transparency of the barriers). Inset in (A): Log-log plot of the average peak spacing $\langle \Delta V_g \rangle$ (solid squares) and its standard deviation $\delta(\Delta V_g)$ (open circles) as a function of D. Linear ($\langle \Delta V_g \rangle \propto 1/D$, solid line) and quadratic [$\delta(\Delta V_g) \propto 1/D^2$, dashed] dependences are plotted as guides to the eye. The dotted curve is the best fit for the average peak spacing: $\langle \Delta V_g \rangle \propto 1/D^\gamma$ yielding $\gamma \approx 1.25$.

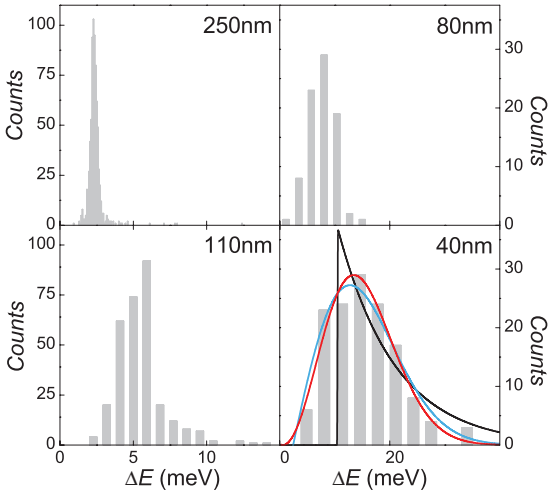

Fig. 3. Level statistics in Dirac billiards. Histograms of the nearest-neighbor level spacing in QDs of different D. The spacing is given directly in terms of ΔE (rather than ΔV_g), which was achieved by measuring the size of Coulomb diamonds. This allows the straightforward comparison between the experiment and theory (*25*). The level statistics becomes increasingly non-Poissonian for smaller QDs. This is illustrated for the smallest device where the red, black, and blue curves are the best fits for the Gaussian unitary, Poisson, and Gaussian orthogonal ensembles, respectively. There are no states at low ΔE because the measured distributions are shifted from the origin due to CB (E_c is used as a fitting parameter).

degeneracy at large n and l, and the number of states around a given energy is proportional to the dot area $\propto D^2$. This effect is often referred to as the level repulsion, a universal signature of quantum chaos. The observed random spacing of CB peaks, random height of Coulomb diamonds, changes in $\langle \Delta V_g \rangle$ quicker than $1/D$ and, especially, the pronounced broadening of the spectral distribution all indicate that chaos becomes a dominant factor for small QDs.

To corroborate this further, Fig. 3 shows that the observed level spacing is well described by Gaussian unitary distribution $(32/\pi^2)\delta E^2 \exp(-4\delta E^2/\pi)$ (characteristic of chaotic billiards) rather than the Poisson statistics $\exp(-\delta E)$ expected for integrable geometries (*25*, *26*). The CB energy shifts the statistical distributions from zero (we measure $\Delta E = E_c + \delta E$ rather than δE), and this makes it difficult to distinguish between unitary and orthogonal ensembles. Nevertheless, the Gaussian unitary distribution fits our data notably better. This agrees with the theory that expects random edges to break down the sublattice symmetry (*27*) leading to the unitary statistics (*25*). In terms of statistics, Dirac billiards are different from the chaotic wave systems that mimic quantum mechanics and are also described by the linear dispersion relation (optical, microwave, and acoustic cavities) but typically obey the Gaussian orthogonal statistics (*28*). Further evidence for the level repulsion in small QDs is provided by the absence of any apparent bunching in their spectra (Fig. 2C). Indeed, despite considerable effort, we did not find repetitive quartets or pairs of CB peaks, which in principle could be expected due to spin and/or valley degeneracy. The latter degeneracy is lifted by edge scattering (*27*), whereas the spin degeneracy may be removed by scattering on localized spins due to broken carbon bonds (*5*).

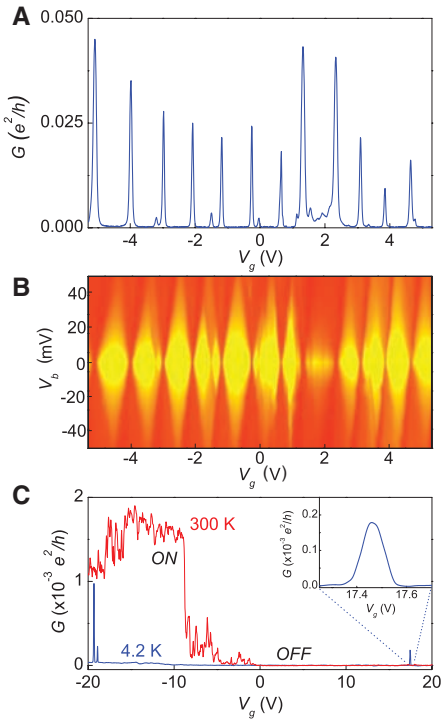

Fig. 4. Electron transport through nm-scale graphene devices. CB peaks (**A**) and diamonds (**B**) for a QD with an estimated size ~ 15 nm. (**C**) Electron transport through a controllably narrowed device with a minimal width of only ≈1 nm as estimated from its ΔE. Its conductance can be completely pinched-off even at room T. Fluctuations in the on state at room T are time dependent (excess noise). At low T, the on state exhibits much lower G, and the noise disappears. Occasional transmission resonances can also be seen as magnified in the inset.

For even smaller devices (D < 30nm), the experimental behavior is completely dominated by quantum confinement. They exhibit insulating regions in V_g sometimes as large as several V, and their stability diagrams yield the level spacing exceeding ~50 meV (Fig. 4, A and B). However, because even the state-of-the-art lithography does not allow one to control features <10 nm in size, the experimental behavior varies widely, from being characteristic of either an individual QD or two QDs in series or an individual QPC (*13*). It is also impossible to relate the observations with the exact geometry because scanning electron and atomic force microscopy fail in visualizing the one-atom-thick elements of several nm in size and often covered by PMMA or its residue. Nevertheless, we can still use δE to estimate the spatial scale involved. Basic arguments valid at a microscopic scale require $a/D \approx \delta E/t$ (where a is the interatomic distance, and $t \approx 3$ eV is the hopping energy), which again yields $\delta E \approx \alpha/D$ with $\alpha \approx 0.5$ eV nm. For example, for the QD shown in Fig. 4 with $\Delta E \approx$ 40 meV, we find $D \sim 15$ nm.

Finally, we used our smallest devices (both QDs and QPCs) to increase δE by further decreasing their size using plasma etching. Some of the devices become overetched and stop conducting, but in other cases we have narrowed them down to a few nm so that they exhibit the transistor action even at room T (Fig. 4C). The device shown appears completely insulating, with no measurable conductance ($G < 10^{-10}$ S) over an extended range of V_g (>30 V) (off state), but then it suddenly switches on, exhibiting rather high $G \approx 10^{-3} e^2/h$. At large biases, we observe the conductance onset shifting with V_b (*13*), which allows an estimate for ΔE as ≈0.5 eV. This value agrees with the T dependence measured near the onset of the on state, which shows that we do not deal with several QDs in series [as it was argued to be the case for nanoribbons (*29*)]. With no possibility to control the exact geometry for the nm sizes, we cannot be certain about the origin of the observed switching. Also, the exact boundary arrangements (armchair versus zigzag versus random edge and the termination of dangling bonds) can be important on this scale (*5*–*12*). Nevertheless, $\delta E \sim 0.5$ eV again allows us to estimate the spatial scale involved in the confinement as only ~1 nm.

Our work demonstrates that graphene QDs are an interesting and versatile experimental system allowing a range of operational regimes from conventional single-electron detectors to Dirac billiards, in which size effects are exceptionally strong and chaos develops easily. Unlike any other material, graphene remains mechanically and chemically stable and highly conductive at the scale of a few benzene rings, which makes it uniquely suitable for the top-down approach to molecular-scale electronics.

References and Notes

1. A. K. Geim, K. S. Novoselov, *Nat. Mater.* **6**, 183 (2007).
2. A. H. Castro Neto, F. Guinea, N. M. R. Peres, K. S. Novoselov, A. K. Geim, *Rev. Mod. Phys.*, in press; preprint at http://xxx.lanl.gov/abs/0709.1163 (2007).
3. M. Y. Han, B. Ozyilmaz, Y. B. Zhang, P. Kim, *Phys. Rev. Lett.* **98**, 206805 (2007).
4. P. Avouris, Z. H. Chen, V. Perebeinos, *Nat. Nanotechnol.* **2**, 605 (2007).
5. Y. W. Son, M. L. Cohen, S. G. Louie, *Nature* **444**, 347 (2006).
6. D. Gunlycke, D. A. Areshkin, C. T. White, *Appl. Phys. Lett.* **90**, 142104 (2007).
7. L. Yang, C. H. Park, Y. W. Son, M. L. Cohen, S. G. Louie, *Phys. Rev. Lett.* **99**, 186801 (2007).
8. N. M. R. Peres, A. H. Castro Neto, F. Guinea, *Phys. Rev. B* **73**, 195411 (2006).
9. V. Barone, O. Hod, G. E. Scuseria, *Nano Lett.* **6**, 2748 (2006).
10. L. Brey, H. A. Fertig, *Phys. Rev. B* **73**, 235411 (2006).
11. B. Wunsch, T. Stauber, F. Guinea, *Phys. Rev. B* **77**, 035316 (2008).
12. I. Martin, Y. M. Blanter, preprint at http://lanl.arxiv.org/abs/0705.0532 (2007).
13. See supporting material on *Science* Online.
14. K. K. Likharev, *Proc. IEEE* **87**, 606 (1999).
15. L. P. Kouwenhoven *et al.*, in *Mesoscopic Electron Transport*, L. L. Sohn, L. P. Kouwenhoven, G. Schön, Eds. (Kluwer Series E345, Dordrecht, Netherlands, 1997), pp. 105–214.
16. E. A. Dobisz, S. L. Brandow, R. Bass, J. Mitterender, *J. Vac. Sci. Technol. B* **18**, 107 (2000).
17. B. Gelmont, M. S. Shur, R. J. Mattauch, *Solid State Electron.* **38**, 731 (1995).
18. J. S. Bunch, Y. Yaish, M. Brink, K. Bolotin, P. L. McEuen, *Nano Lett.* **5**, 287 (2005).
19. F. Miao *et al.*, *Science* **317**, 1530 (2007).
20. C. Stampfer *et al.*, *Appl. Phys. Lett.* **92**, 012102 (2008).
21. U. Sivan *et al.*, *Phys. Rev. Lett.* **77**, 1123 (1996).
22. S. R. Patel *et al.*, *Phys. Rev. Lett.* **80**, 4522 (1998).
23. P. G. Silvestrov, K. B. Efetov, *Phys. Rev. Lett.* **98**, 016802 (2007).
24. I. M. Ruzin, V. Chandrasekhar, E. I. Levin, L. I. Glazman, *Phys. Rev. B* **45**, 13469 (1992).
25. M. V. Berry, R. J. Mondragon, *Proc. R. Soc. London A* **412**, 53 (1987).
26. T. Guhr, A. Müller-Groeling, H. A. Weinedmüller, *Phys. Rep.* **299**, 189 (1998).
27. A. Rycerz, J. Tworzydlo, C. W. J. Beenakker, *Nat. Phys* **3**, 172 (2007).
28. U. Kuhl, H.-J. Stöckmann, R. Weaver, *J. Phys. A* **38**, 10433 (2005).
29. F. Sols, F. Guinea, A. H. Castro Neto, *Phys. Rev. Lett.* **99**, 166803 (2007).

30. The research was supported by Engineering and Physical Sciences Research Council (UK), the Royal Society, and Office of Naval Research. We are grateful to K. Ensslin, L. Eaves, M. Berry, L. Vandersypen, A. Morpurgo, A. Castro Neto, F. Guinea, and M. Fromhold for helpful discussions.

Supporting Online Material

www.sciencemag.org/cgi/content/full/320/5874/356/DC1
Materials and Methods
SOM Text
Figs. S1 to S5
References

27 December 2007; accepted 5 March 2008
10.1126/science.1154663

Supplementary Online Material

for paper "Chaotic Dirac Billiard in Graphene Quantum Dots"
by Ponomarenko *et al*

Materials and Methods

Different quantum dot designs

The SEM micrograph in Fig. 1 of the main text shows the basic QD design but is also intended to illustrate the high resolution of our electron-beam lithography that allows features as small as 10 nm to be made reliably. The shown arrangements of side electrodes would be standard for most semiconductor-quantum-dot experiments (*S1*). However, we have found this design to be less efficient for our studies that required sweeps over hundreds of energy levels. Indeed, if we place side gates in the immediate proximity of CIs (like shown in Fig. 1), this limits the number of levels that could be probed inside our smallest QDs usually down to ~10 (spacing between peaks as a function of back-gate voltage could become as large as 10V). We attribute the reduced influence of the back gate to additional strong screening by side electrodes. The adjacent side gates are also not efficient enough to scan over many quantum states because of the electrical breakdown or leakage along the device surface. To probe hundreds of energy levels needed for the analysis presented in the main text, we have often employed the geometry shown in Fig. S1, in which side gates are located ~1 μm away from the CI. The back-gate voltage is swept typically between ±60V (limited by the onset of a leakage current through the gate dielectric), and a distant side gate is used for scans over small energy intervals only.

Graphene-based quantum point contacts

The graphene constrictions that define quantum dots in our experiments were normally designed to have equal length and width w. We have avoided long constrictions as they often result in the development of spurious QDs within individual constrictions (*S2*,*S3*). Wide constrictions (w >40nm) have too high conductance and do not allow Coulomb blockade, whereas narrow ones (w <10nm) exhibit large energy gaps with no measurable conductance (see further) and, therefore, no possibility to probe states inside QDs. From experience, we have found $w \approx$20nm to be most suitable for making quantum barriers with G less but not much less than e^2/h, which is optimal for CB measurements (*S1*). For a reference, Figure S2 shows the typical behavior exhibited by such individual constrictions that can also be referred to as quantum point contacts (QPC). The overall shape of their $G(V_g)$-response resembles $\sigma(V_g)$ for bulk graphene with the neutrality point (NP) shifted by chemical doping (to +50V in Fig. S2).

It is obvious that the behavior of QPCs (with their high G over a large but finite range of gate voltages) limits the operation of our quantum dots to regions of less than ~20V around the G minima, where QPCs remain sufficiently low conductive (compare Figs. 1B and S2).

Individual 20-nm constrictions exhibit mesoscopic (interference) fluctuations as a function of V_g (see Fig. S2) but they are normally smooth on a typical scale of CB oscillations. Also, with increasing bias V_b, $G(V_g)$-curves become smoother with the minimum in $G(V_g)$ becoming increasingly less pronounced, which replicates the behavior observed with increasing T. Importantly, no Coulomb diamonds accompany these fluctuations above 4K, in contrast to the behavior reported for graphene nanoribbons (*S2-S5*) (i.e. in our case, fluctuations decrease in amplitude with increasing V_b rather than broaden). This shows that individual QPCs (together with their source and drain regions) are only responsible for smooth variations in the height of CB peaks (see Fig. 1) and cannot possibly cause random peak positions, which would require several QDs in series of approximately the same size, as in the case of stochastic CB (*S6*) (see below).

Nanometer-sized point contacts

We have also studied QPCs of smaller sizes (design $w \approx 10$ nm). The inset in Figure S3 shows a micrograph for one of such nm-scale devices. With changing gate voltage, they usually exhibit two well-defined regimes: complete pinch-off with conductance below our detection limit of $G < 10^{-10}$ S and a strongly fluctuating finite G. Both regimes persist over extremely large intervals of V_g. This obviously makes so narrow QPCs not suitable for the QD design. Figure S3 shows that fluctuations in the conducting regime are suppressed at finite biases. Again, no diamonds are observed in this regime but instead the amplitude of fluctuations decreases with increasing V_b, which is typical for interference phenomena. In contrast, the pinch-off region gradually becomes narrower with increasing bias V_b so that only one but huge Coulomb diamond could be seen in this regime. For the case of Figure S3, the size of the diamond yields a confinement gap δE of ≈150meV. Note that, after oxygen plasma etching, our QPCs become somewhat narrower (by a few nm) than their designed width of 10nm. We have also measured the T dependence of G in the pinch-off state (inset in Fig. S3) and found an activation gap E_A ~80meV. The latter is approximately twice smaller than the gap found from the size of the diamond, which can be explained by impurity states that "soften" the confinement gap (*S7*).

SOM Text

Excited states in quantum dots

The importance of quantum confinement for graphene-based quantum dots is also witnessed through the presence of excited states on the stability diagrams (*S1*). In Fig. 2B such states are faint (additional lines have to be drawn to indicate them). This is a common case for our quantum dots, in which graphene constrictions rapidly become more conductive under higher applied biases, as described above. Accordingly, Coulomb diamonds' boundaries away from zero V_b are smeared by high transparency of the quantum barriers, which blurs diamonds at high biases (Fig. 2) and leaves little chance for excited states to be observed. However, in some cases, QPCs fortuitously remain resistive enough even at high V_g and excited states could be seen rather clearly (see Fig. S4).

Quantum dots in series and stochastic Coulomb blockade

Although large confinement effects are expected for graphene QDs (as discussed in the main text), we have also considered other mechanisms that could cause random positions of CB peaks. For example, in the case of stochastic CB (*S6*), peaks could become seemingly non-periodic due to the presence of two or more QDs.

The high accuracy of our electron-beam lithography guarantees that there is no accidental additional confinement that would let our devices operate as two or more quantum dots in series and lead to stochastic CB. Indeed, this would require a barrier between two QDs with resistance $\sim h/e^2$, which as shown above is hard to achieve without an additional constriction narrower than ~30 nm. Our high-resolution lithography and following visualization in a scanning electron microscope rule out such constrictions for devices with $D \geq 30$nm (for example, see micrographs in Figs. 1 and S3). Furthermore, electron and hole puddles always present in graphene near the neutrality point (*S8*) cannot be responsible for the observations of random peaks for several reasons. First, barriers between such puddles are expected to be rather transparent because of the Klein tunneling (*S9*). Second, the reported CB peaks extend over a large interval of gate voltages with typically more than one hundred peaks recorded whereas puddles are not deep enough to allow more that a couple of electrons inside (*S8*).

Still, it is instructive to compare the reported chaotic behavior of CB peaks with the one where quantum dots in series cause the stochastic CB. In the latter case, some CB peaks originating from one of the QDs completely disappear due to zero G through the other dots and vice versa (*S6*). The critical signature of two or more QDs in series is not only seemingly random

positions of CB peaks (statistics would still reveal that they are not random) but also accompanying strong variations in their amplitudes (from 100% to a tiny fraction of 1%). Moreover, some peaks that are completely suppressed at low T should appear at higher T as the conductance of the blocking dot increases.

This CB behavior is illustrated in Fig. S5. In this case, because of a mistake in lithography, a relatively large QD appeared in series with a smaller QD ($D \approx$20nm) inside one of the barriers (as later found in SEM). One can see a seeming random pattern of CB peaks in Fig. S5. However, more careful inspection reveals that many of the peaks have a common spacing, and most of the larger gaps correspond to the double spacing, which suggests one of the peaks missing. When we increase T or V_g, the missing peaks dutifully reveal themselves, as expected for stochastic CB (*S6*). This behavior of double QDs is in stark contrast to the one observed in our small individual QDs, in which – despite the absence of periodicity – CB peaks exhibit only smooth variations in their height, no additional peaks appeared at higher biases or with increasing T and, probably most convincingly, the T dependence of CB was in agreement with the measured size of Coulomb diamonds.

Supporting Figures and Legends

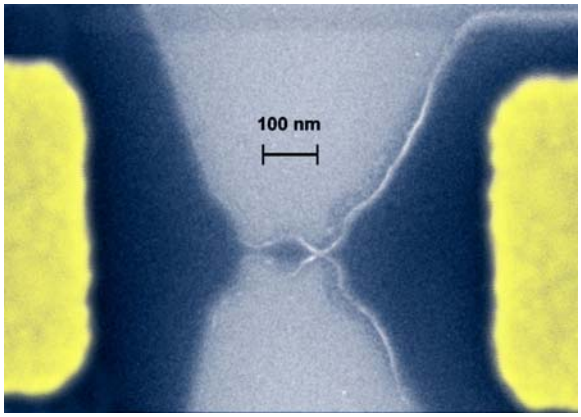

Figure S1. The scanning electron micrograph (in false color) illustrates the most typical design of our quantum dot devices. In this case ($D \approx$80nm), side-gate electrodes are remote and outside the visible frame. Their removal from the immediate vicinity of the CI significantly improves its coupling to the back gate allowing scans over hundreds rather than dozens of CB peaks. Dark areas in the SEM micrograph are the PMMA mask that protected graphene during plasma etching so that it is left only underneath the mask. Yellowish regions are Au/Ti contacts.

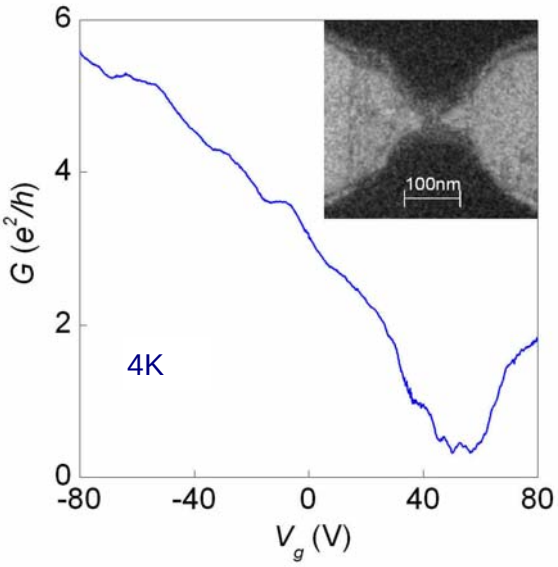

Figure S2. Conductance of an individual 20-nm graphene constriction, similar to those used in our quantum dots. Making them short and narrow has ensured that no spurious quantum dots were present inside the barriers.

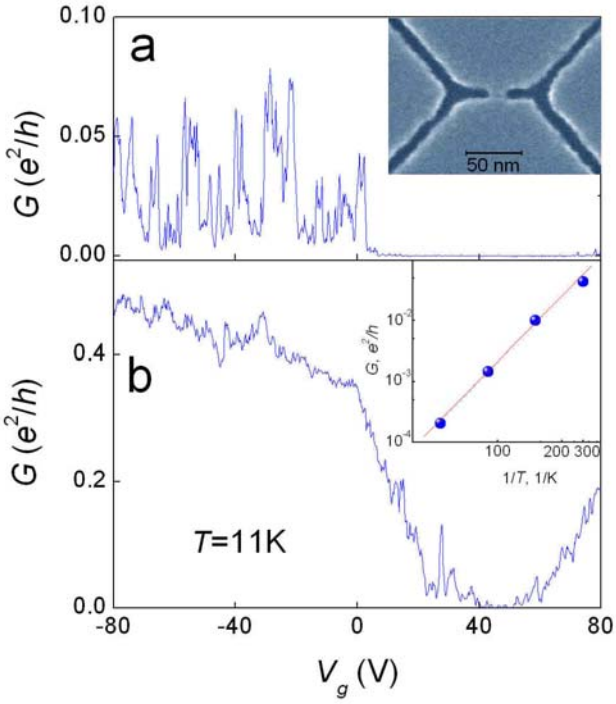

Figure S3. Electron transport through 10-nm graphene constrictions. (**a,b**) – conductance G as a function of back-gate voltage at zero and 100 mV bias, respectively. Mesoscopic fluctuations in the conducting regime become suppressed, whereas the pinch-off region becomes narrower, indicating a large confinement gap. Inserts: (**a**) – SEM micrograph of one of our narrow QPCs (before plasma etching); and (**b**) – G in the pinch-off region ($V_g \approx 40$V) can be fitted by the activation T dependence $G \propto \exp(-E_A/2T)$.

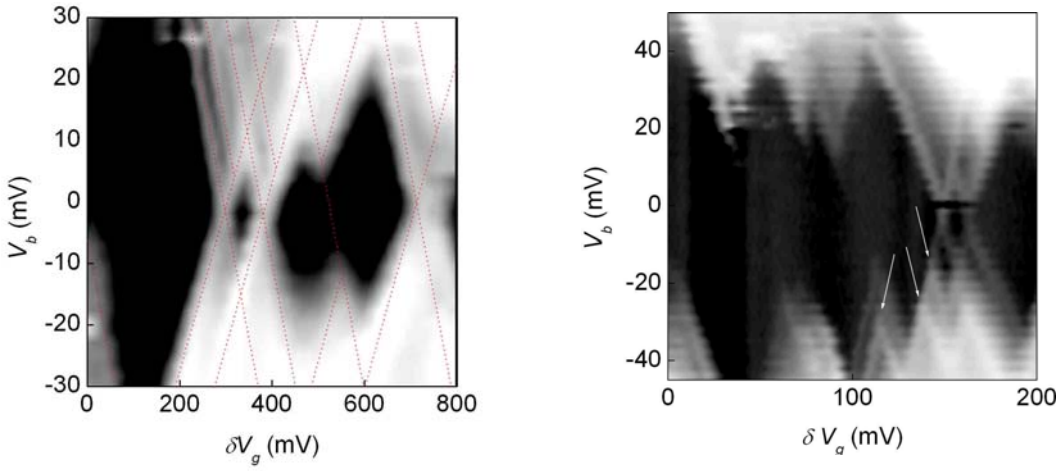

Figure S4. Examples of excited states as observed for two different quantum dots, when the barriers remained low conductive (<0.5 e^2/h) even at high biases. The red dashed lines (left figure) and small white arrows (on the right) are guides to the eye.

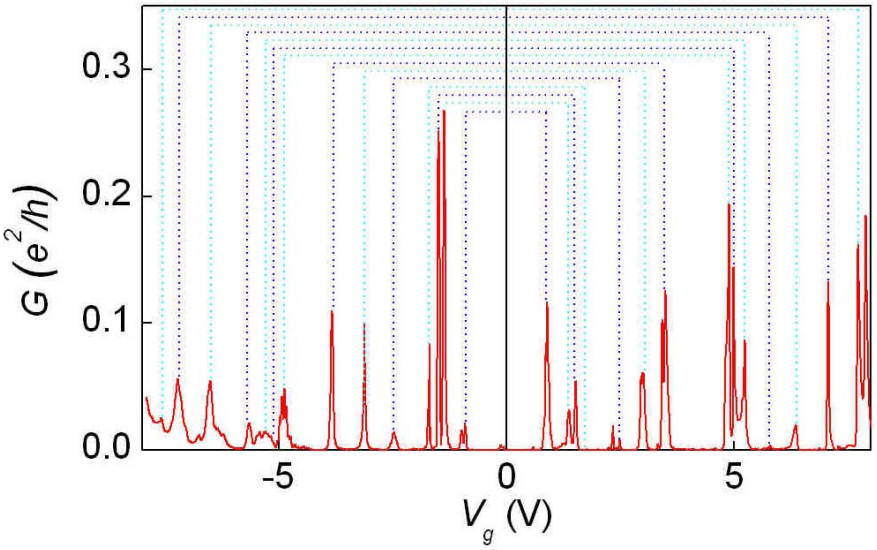

Figure S5. Stochastic Coulomb blockade. Two quantum dots in series can lead to seemingly random peaks because some of them essentially disappear whereas others have tiny amplitudes. We also note that, in rare cases, we succeeded in finding certain symmetry for electron and hole peaks. This is the case of this particular device, where the neutrality point (revealed by a clear minimum in G at room T) is at $V_g \approx 0$V and the peaks are positioned symmetrically with respect to NP as indicated by dotted lines.

Supporting references

S1. L. P. Kouwenhoven *et al*, in *Mesoscopic Electron Transport*, edit. by L. L. Sohn, L. P. Kouwenhoven, G. Schön (Kluwer Series E345) p. 105-214 (1997).

S2. B. Ozyilmaz, P. Jarillo-Herrero, D. Efetov, P. Kim. *Appl. Phys. Lett.* **91**, 192107 (2007).

S3. F. Sols, F. Guinea, A. H. Castro Neto. *Phys. Rev. Lett.* **99**, 166803 (2007).

S4. M. Y. Han, B. Ozyilmaz, Y. B. Zhang, P. Kim. *Phys. Rev. Lett.* **98**, 206805 (2007).

S5. P. Avouris, Z. H. Chen, V. Perebeinos. *Nature Nanotech.* **2**, 605 (2007).

S6. I. M. Ruzin, V. Chandrasekhar, E. I. Levin, L. I. Glazman, *Phys. Rev. B* **45**, 13469 (1992).

S7. D. Basu, M.J. Gilbert, L.F. Register, A.H. MacDonald, S.K. Banerjee. arXiv:0712.3068.

S8. J. Martin *et al*. *Nature Phys*. **4**, 144 (2008).

S9. A. K. Geim, K. S. Novoselov. *Nature Mater*. **6**, 183 (2007).